https://doi.org/10.5194/egusphere-2026-2853
Preprint. Discussion started: 5 June 2026

From snow wetting to pond formation: Stage-resolved L-band sea ice roughness during the Arctic melt season

Suna Jo[1], Sungwook Hong[2,3]

[1]Department of Environment and Energy, Sejong University, Seoul, 05006, Republic of Korea
[2]Department of Environment and Energy, Center for Earth and Environment Research, Sejong University, Seoul, 05006, Republic of Korea
[3]DeepThoTh Company Ltd., Seoul, 05006, Republic of Korea

Correspondence to: Sungwook Hong (sesttiya@sejong.ac.kr)

Abstract. Arctic summer surface evolution is commonly characterized using optical melt pond fraction, but optical retrievals are limited by persistent cloud cover and cannot resolve internal snow–ice changes that occur before ponds become visible. L-band passive microwave observations are largely unaffected by clouds and respond to near-surface dielectric changes within the snow and upper ice layer, suggesting their potential to detect pre-pond surface transitions. This study examines whether small-scale L-band sea ice roughness (L-SIR), retrieved from Soil Moisture Active Passive brightness temperatures, provides a physically consistent precursor to optically detectable melt pond development. Using observations from 2017 to 2023 over a multiyear ice region in the central Arctic, we analyze the temporal ordering among the transition to positive net surface energy flux, the L-SIR transition, and melt pond formation, together with stage-dependent relationships between L-SIR and surface energy balance variables. The L-SIR transition occurs approximately two weeks after the net surface energy flux becomes positive and approximately four weeks before melt pond formation, with this ordering reproduced across years and latitudes. Correlations with surface energy variables also change systematically across three stages, shifting from a temperature-related regime to a latent heat- and longwave-associated regime during active snow ablation and meltwater redistribution, and finally to a pond coverage-related regime. These results indicate that L-SIR provides a complementary satellite-derived product for characterizing pre-pond Arctic summer surface evolution that is not captured by optical melt pond fraction alone.

1 Introduction

Arctic sea ice has undergone a pronounced decline since satellite observations began in 1979, with September ice extent decreasing at a rate of approximately 13 % per decade and surface temperatures (Ts) increasing at four times the global mean rate (Rantanen et al., 2022; Serreze and Meier, 2019; Stroeve et al., 2014). This rapid transformation is driven by ice albedo feedback, in which retreating sea ice progressively exposes darker ocean and meltwater surfaces, increasing solar absorption and accelerating further melt. Within this feedback chain, melt ponds are among the most thermodynamically influential surface features of the Arctic summer (Aparício, 2023). Their albedo, typically in the range of 0.15 to 0.45, results in

https://doi.org/10.5194/egusphere-2026-2853
Preprint. Discussion started: 5 June 2026

substantially greater absorption of solar radiation than over bare or snow-covered ice, and melt rates beneath ponded surfaces can be two to three times higher than beneath adjacent unponded ice (Fetterer and Untersteiner, 1998; Lüthje et al., 2006; Perovich and Polashenski, 2012; Skyllingstad et al., 2009).

Melt pond fraction (MPF), defined as the ratio of ponded area to the total sea ice surface area, has become the primary quantitative descriptor of pond extent and a key variable for constraining albedo parameterizations in sea ice and climate models (Eicken et al., 2004; Flocco et al., 2012; Landy et al., 2014; Niehaus et al., 2023) Early-season pond dynamics also carry predictive skill for September sea ice extent, thereby establishing MPF as a potentially valuable seasonal forecast variable (Liu et al., 2015; Schröder et al., 2014). Satellite observations indicate a statistically significant increase in pan-Arctic MPF since the early 2000s that is associated with earlier melt onset and a progressively longer melt season (Feng et al., 2022). The incomplete representation of melt pond processes remains a recognized source of uncertainty in simulations of Arctic sea ice evolution, which makes accurate characterization of MPF and its seasonal variability all the more pressing (Diamond et al., 2024; Niehaus et al., 2024).

At the pan-Arctic scale, MPF retrieval relies primarily on satellite observations, with optical sensors providing the most widely used datasets (Ding et al., 2020; Niehaus et al., 2024; Rösel et al., 2012). However, this approach is fundamentally limited by its dependence on clear-sky conditions, because Arctic summers are persistently overcast, disrupting temporal continuity and potentially obscuring the detection of melt pond onset over periods of days to weeks (Aparício, 2023; Istomina et al., 2025; Walsh et al., 2009). In addition, MPF is inherently a two-dimensional metric that captures only the areal extent of ponding, and it cannot directly resolve earlier internal changes in ice state that precede visible pond formation, such as the accumulation of liquid water within the snowpack and the development of ice permeability (Eicken et al., 2002; Mortin et al., 2016; Stroeve et al., 2014). Passive microwave observations offer a complementary perspective that addresses these limitations. In particular, L-band (1.4 GHz) measurements are largely unaffected by cloud cover, and their longer wavelength and greater penetration depth than higher-frequency microwave bands make them sensitive to near-surface dielectric changes that occur within the snow and upper ice layer (Arndt et al., 2016; Kaleschke et al., 2012; Maaß et al., 2013). These properties suggest that L-band measurements may carry information about pre-ponding surface transitions that are not accessible through optical sensors.

Small-scale sea ice roughness (SIR) is retrieved from polarization differences in brightness temperatures through a semi-empirical inversion of a rough surface reflectivity model (Hong, 2010; Hong and Shin, 2010). These studies have shown that SIR is sensitive to changes in the near-surface dielectric properties of the ice as it transitions from cold, dry conditions to moist, thermodynamically active states. Applying this framework to Soil Moisture Active Passive (SMAP) satellite observations, Jo et al. (2019) further demonstrated that L-band SIR (L-SIR) responds systematically to thin ice variability, suggesting that microwave-derived roughness can capture surface transitions that are not detectable through optical observations. However, L-SIR should not be interpreted as a direct proxy for MPF. It instead reflects an internal ice state transition that precedes visible pond development. This view is consistent with previous studies showing that pond formation is governed not only by surface wetting but also by the surface energy balance. In particular, Skyllingstad and Polashenski

https://doi.org/10.5194/egusphere-2026-2853
Preprint. Discussion started: 5 June 2026

(2018) demonstrated that pond onset is closely linked to the transition of the net surface heat flux from negative to positive, with turbulent heat fluxes playing a dominant triggering role. Under this framework, surface wetting and internal structural modification can already be underway before the cumulative surface energy becomes sufficient to sustain optically detectable ponds.

In this study, we investigate whether the onset of L-SIR decline, defined as a sustained decrease in the SIR time series, can serve as a physically consistent precursor to the active stage of optically detectable melt pond development. Using seven years of observations (2017–2023) at a fixed multiyear ice region in the central Arctic, we analyze how the relationships between L-SIR and MPF, as well as between L-SIR and key surface energy balance variables, evolve across distinct melt phases. The objective is not to predict the precise date of pond formation. Rather, we aim to demonstrate that L-SIR captures a physically meaningful internal transition preceding pond formation that is systematically linked to the surface energy balance conditions governing the eventual emergence of melt ponds, and that the L-SIR signal reflects physically distinct surface processes across successive phases of the melt season.

2 Study area and Data

2.1 Study area

The study area is located in the central Arctic (84–85.5° N, 50–70° W), a region where some of the thickest multiyear ice in the Arctic is found (Lange et al., 2018; Fig. 1). This region was selected because it maintains stable sea ice cover throughout the summer without undergoing complete seasonal ice loss, and because cloud contamination of the optical MPF dataset is minimized, providing relatively continuous temporal coverage. Such conditions are rare across the Arctic, making this region

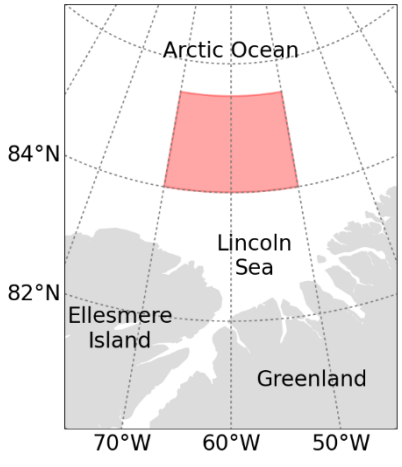

Figure 1: Study area in the central Arctic. The red polygon indicates the analysis domain bounded by 84–85.5°N and 50–70°W, located near the Lincoln Sea.

https://doi.org/10.5194/egusphere-2026-2853
Preprint. Discussion started: 5 June 2026

one of the few locations where both continuous ice coverage and sufficient observational continuity are achievable. Niehaus et al. (2025) showed that the MPF product used in this study exhibits low spatiotemporal inhomogeneity over the central Arctic, supporting the use of this site for stable analysis. The analysis was conducted over seven melt seasons from 2017 to 2023, spanning 4 May to 27 September each year. During this period, sea ice conditions derived from the Arctic Ocean Sea Ice Reanalysis (Williams et al., 2021) of the E.U. Copernicus Marine Environment Monitoring Services (CMEMS) indicated that the mean sea ice concentration at the site was 97.2 % (minimum 74.5 %), the mean sea ice age was 3.26 years (minimum 2.3 years), and the mean sea ice thickness was 3.0 m (minimum 0.47 m).

2.2 MPF Data

The MPF dataset used in this study is the Melt Pond Detection 2 (MPD2) product developed by the University of Bremen, which provides one of the few continuous multiyear MPF records available for the Arctic (Niehaus et al., 2024). The MPD2 algorithm is based on reflectance measurements from eight spectral bands in the visible and near-infrared range (412–885 nm) acquired by the Sentinel-3 Ocean and Land Colour Instrument, with additional cloud screening performed using observations from the Sentinel-3 Sea and Land Surface Temperature Radiometer. The dataset has a reported uncertainty of 7.8 % and a bias of 1.6 %. The MPD2 product has been available since 2017 for regions north of 60° N at a spatial resolution of 12.5 km. Both daily and weekly composites are provided. However, because daily data are strongly affected by cloud filtering, the weekly composite product was used in this study. These weekly composites are currently available only through 2023.

2.3 SMAP Brightness Temperatures

To derive L-SIR, brightness temperatures from SMAP mission (Entekhabi et al., 2010) were used, including both vertically and horizontally polarized brightness temperatures. Since its launch on 31 January 2015, SMAP has been widely used for various cryospheric applications, including permafrost monitoring, sea ice classification, and salinity estimation. The SMAP radiometer operates at L-band (1.41 GHz) and uses a conically scanning antenna with a fixed incidence angle of approximately 40°. To mitigate radio frequency interference, the SMAP radiometer employs a combination of detection methods, including pulse detection, cross-frequency analysis, kurtosis detection, and polarization-dependent thresholding (Mohammed et al., 2016; Piepmeier et al., 2014).

In this study, the Level-3 enhanced brightness temperature product version 6 was obtained from the NASA National Snow and Ice Data Center (O'Neill et al., 2023). The data are provided on the EASE-Grid 2.0 projection at a spatial resolution of 9 km and cover the period from 31 March 2015 onward (O'Neill et al., 2021). To ensure consistency with the MPD2 dataset, the SMAP data were resampled to a 12.5 km grid. Both ascending (18:00 local solar time) and descending (06:00 local solar time) overpasses were used. To reduce spatial data gaps and obtain more complete daily coverage over the study area, brightness temperatures from both passes were averaged to produce daily vertically and horizontally polarized polarized brightness temperatures. Quality assessment flags were applied to retain only observations of acceptable quality.

https://doi.org/10.5194/egusphere-2026-2853
Preprint. Discussion started: 5 June 2026

2.4 CMEMS Ts

Ts was used as an additional key input variable for the L-SIR retrieval. For this purpose, we employed the Arctic Ocean Sea and Ice Surface Temperature Level-4 reprocessed product distributed by the CMEMS (Karagali et al., 2025). This product provides a daily, satellite-based Arctic Ts analysis generated by the Danish Meteorological Institute through an Optimal Interpolation system. The analysis encompasses the Arctic Ocean north of 58° N and incorporates Ts estimates over the open ocean, marginal ice zone, and sea ice. Within this framework, Ts observations are combined with sea ice concentration and land mask to produce a spatially gap-free daily dataset. Over sea ice, the ice surface temperature (IST) component is derived from thermal infrared Advanced Very High Resolution Radiometer observations compiled from two internally consistent satellite data streams: the Arctic and Antarctic IST from thermal Infrared satellite climate dataset version 2, which covers 1982–2014, and the OSI SAF OSI-205 product, which covers 2015 onward. At the time of analysis, the product record spanned 1 January 1982 through 31 December 2024 and was updated annually as upstream observational data became available. The product was resampled from its native 0.05° grid to the 12.5 km resolution adopted for the L-SIR retrieval.

2.5 ERA5 Dataset

To examine how the relationship between L-SIR and key surface energy variables evolves during the melt season, data were obtained from the European Centre for Medium-Range Weather Forecasts Reanalysis version 5 (ERA5) (Hersbach et al., 2020). The ERA5 dataset provides a physically consistent, long-term record of atmospheric and surface conditions at a temporal resolution of 1 h and a spatial resolution of 0.25°. The variables used in this study included mean surface radiative and heat fluxes, specifically latent heat (LH), sensible heat (SH), net longwave radiation (LW_{net}), net shortwave radiation (SW_{net}), downward longwave radiation (LWD), and downward shortwave radiation (SWD), as well as 2 m air temperature (T_{2m}), and Ts. In ERA5, surface fluxes follow the convention that positive values are directed downward. These variables collectively characterize the dominant terms of the Arctic surface energy balance during the melt season (Mortin et al., 2016; Skyllingstad et al., 2015; Taylor and Feltham, 2004). For consistency with the temporal scale of the L-SIR and MPF analyses, ERA5 data at 00, 06, 12, and 18 UTC were averaged to produce daily mean values.

3 Methods

3.1 L-SIR Retrieval

The L-SIR was retrieved using the semi-empirical incoherent passive microwave roughness framework established by Hong (2010) and subsequently applied in Hong and Shin (2010) and Jo et al. (2019). In this approach, polarized rough surface reflectivities derived from satellite brightness temperatures were used as inputs to the retrieval equation. The resulting parameter represents an effective small-scale roughness associated with the L-band microwave response of near-surface sea ice, rather than large-scale surface relief such as pressure ridges or deformation features. For each polarization *P*, where *P*

https://doi.org/10.5194/egusphere-2026-2853
Preprint. Discussion started: 5 June 2026

denotes either vertical or horizontal polarization, the rough surface reflectivity was calculated following Comiso et al. (2003) as:

$$R_{P,rough} = 1 - \frac{T_{B,P}}{Ts}, \quad (1)$$

where TB denote the observed SMAP polarized brightness temperatures, and Ts is obtained from the Copernicus Marine Service product described in Sect. 2.4. The L-SIR was then estimated as:

$$L\text{-}SIR = \frac{\lambda}{4\pi\cos\theta} \cdot \sqrt{ln\left(\frac{R_{H,rough}{}^{sec^2\theta}}{R_{V,rough}}\right)}, \quad (2)$$

The SMAP wavelength (λ) and fixed incidence angle (θ) were set to 21.43 cm and 40°, respectively. This expression was obtained by combining the Gaussian surface height distribution model of Choudhury et al. (1979), which relates rough surface reflectivity to its specular counterpart through an exponential damping term, with the Hong approximation ($R_{V,spec} = R_{H,spec}{}^{sec^2\theta}$; Hong, 2009). The Hong approximation establishes a relationship between vertically and horizontally polarized specular reflectivities without requiring a priori knowledge of the complex refractive index. Together, these two components allow the specular reflectivity terms to be eliminated, expressing the retrieval entirely in terms of satellite-observable rough surface reflectivities. The retrieved L-SIR values generally ranged from approximately 0 to 2 cm.

3.2 Definition of key transition dates

To delineate physically distinct phases of the melt season and provide consistent temporal references for the subsequent analyses, five key transition dates were identified at each pixel for every year of the study period. These dates were (1) the positive net surface energy flux (F_{net}) transition date, (2) the L-SIR transition date, (3) the melt pond formation date, and the (4) start and (5) end dates of the melt season. Among these, the positive F_{net} transition date, the L-SIR transition date, the melt pond formation date, and the melt season end date define three successive melt season stages used in the stage-resolved analysis. These stages were used as temporal references for examining how the characteristics of L-SIR varied across each stage.

3.2.1 Positive F_{net} transition date

The F_{net} into the snow–ice surface was defined as:

$$F_{net} = LW_{net} + SW_{net} + LH + SH + C, \quad (3)$$

where SW_{net} and LW_{net} were obtained from their downward and upward components, and C denotes the upward conductive heat flux. The radiative and turbulent fluxes were taken from ERA5, and all fluxes were expressed under a downward-positive convention. Although C can be an important component of the surface energy budget during winter, it becomes

https://doi.org/10.5194/egusphere-2026-2853
Preprint. Discussion started: 5 June 2026

small near melt onset as the temperature gradient within the snow–ice column weakens and the snowpack approaches an isothermal state (Else et al., 2014). Persson (2012) estimated C to be approximately 2 W m−2 near melt onset over multiyear ice. Because the present study aims to compare atmospheric surface forcing with L-SIR variability rather than to close the full surface energy budget, the conductive term was not explicitly evaluated. The F_{net} used here therefore corresponds to the atmospheric component of the surface energy balance, with C omitted. Positive F_{net} indicates net energy gain by the snow–ice surface system, and its transition to positive values has been linked to spring melt pond onset (Persson, 2012; Skyllingstad and Polashenski, 2018). Therefore, to suppress transient sign reversals, the positive F_{net} transition date was defined as the first date when the 3-day running mean of F_{net} remained positive.

3.2.2 L-SIR transition date

The second date was defined as the L-SIR transition date, representing the first major seasonal-scale change in L-SIR during the early melt season. This timing is hereafter referred to as L-SIR onset. Because L-SIR is sensitive to short-term variability, a 7-day running mean was first applied to the time series to reduce minor oscillations. The L-SIR onset date was then operationally defined as the date of the first prominent local peak in the smoothed time series, identified using a prominence threshold equal to one standard deviation. This peak corresponds to the turning point that precedes the seasonal decline in L-SIR and was used to isolate the first major L-SIR transition.

3.2.3 Melt pond formation date

The third date marks the onset of optically detectable melt ponds. We adopted the threshold-based approach of Niehaus et al. (2025), who used the same MPD2 product and defined pond formation relative to the retrieval uncertainty of the algorithm. The reported MPD2 uncertainty of 7.8 % was used as the threshold, on the rationale that values exceeding this level can be interpreted as a physically meaningful pond signal rather than retrieval noise. A 3-day running mean was first applied to the MPF time series, and the melt pond formation date was defined as the first date on which the smoothed MPF exceeded 7.8 %. This timing is hereafter referred to as MPF onset.

3.2.4 Melt season start and end dates

The start and end of the melt season were defined following Persson (2012), in which the onset and termination of summer melt were identified using Ts and near-surface air temperature. Specifically, the melt season was defined as the interval bounded by the first and final occurrences when either Ts or T_{2m} exceeding -0.1 °C within a given year. In this study, the Ts and T_{2m} were taken from ERA5, and a 3-day running mean was applied before using this criterion.

https://doi.org/10.5194/egusphere-2026-2853
Preprint. Discussion started: 5 June 2026

4 Results

Figure 2 shows the 3-day running mean time series of L-SIR, MPF, F_{net}, Ts and T_{2m} at 84.25° N, 60° W during the 2023 melt season, with the smoothing applied to suppress short-lived fluctuations. Key transition dates, identified according to the criteria described in Section 2, overlaid on the time series. The first sustained positive transition in F_{net} occurs on 27 May, followed by L-SIR onset on 12 June and MPF onset on 28 June, as indicated by the black, red, and blue dashed lines, respectively. The yellow shading denotes the melt season, from 5 June to 28 August. The three transition dates reveal a clear sequential structure. F_{net} becomes positive approximately two weeks before L-SIR onset, and L-SIR onset precedes MPF onset by another two weeks. This timing indicates that positive net energy input does not immediately lead to optically detectable ponding (Eicken et al., 2002; Skyllingstad and Polashenski, 2018). Instead, L-SIR responds during a pre-ponding transition, as Ts and T_{2m} approach the melting point and the snow–ice surface likely undergoes thermal and dielectric changes (Mortin et al., 2016; Persson, 2012). This earlier response implies that L-SIR captures surface transformation before sufficient meltwater has accumulated and pooled into optically detectable ponds. After melt pond formation, L-SIR and MPF vary in opposite directions, particularly during July and August. This shift suggests that L-SIR reflects different surface conditions before and after the development of melt ponds. Collectively, the sequential transitions in F_{net}, L-SIR, and MPF delineate three physically meaningful intervals, which were used to define three stages for the subsequent analyses. Stage 1 spans the period from the Positive F_{net} transition date to L-SIR onset, stage 2 spans the period from L-SIR onset to MPF

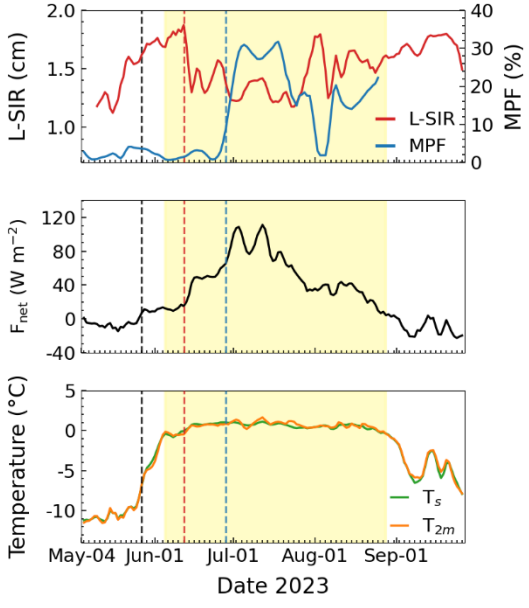

Figure 2: 3-day running mean time series of L-SIR, MPF, F_{net}, Ts and T_{2m} during the 2023 melt season at 84.25°N, 60°W. The black, red, and blue dashed lines indicate the positive Fnet transition, L-SIR onset, and MPF onset dates, respectively. The yellow shading denotes the melt season.

https://doi.org/10.5194/egusphere-2026-2853
Preprint. Discussion started: 5 June 2026

onset, and stage 3 spans the period from MPF onset to the end of the melt season.

The temporal ordering described above was not limited to a single year or location. Figure 3 shows the mean timing of five transition dates from 2017 to 2023 as a function of latitude between 84° N and 85.5° N. Although the absolute dates varied from year to year, the overall progression from the positive F_{net} transition to early-season L-SIR onset and melt start, MPF onset, and melt season end was preserved across all years and latitudes. Within individual years, the timing of each event showed only modest latitudinal variation, indicating that the seasonal transition progressed coherently across the study region. The domain-mean timing was broadly consistent with the central Arctic melt pond chronology reported by Niehaus et al. (2025). Although our study area covered only one sector of the central Arctic, both studies indicate that melt conditions generally begin around early June and that pond formation follows in early July. Averaged across the 7-year period, L-SIR

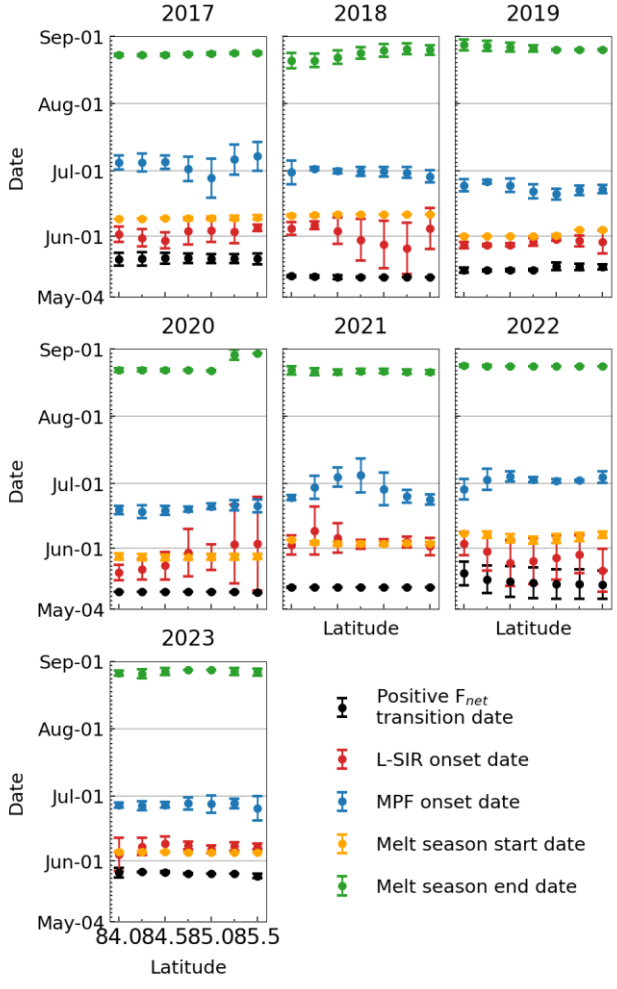

Figure 3: Latitudinal variation in melt-season transition timing from 2017 to 2023. The transitions include positive Fnet transition, L-SIR onset, MPF onset, melt-season start, and melt-season end. Markers denote the mean timing at each latitude, and error bars indicate the standard deviation.

https://doi.org/10.5194/egusphere-2026-2853
Preprint. Discussion started: 5 June 2026

onset occurred approximately 14 days after the positive transition of F_{net}, and MPF onset followed L-SIR onset by an additional 27 days. The relative timing of L-SIR onset and the melt season start date varied modestly from year to year. In 2020, 2021, and 2023, the two events occurred nearly simultaneously, whereas in the remaining years, L-SIR onset occurred before melt start. This suggests that the two indicators capture related, but not identical, components of the early-summer sea ice transition. Localized cases with large standard deviations were observed, including near 85° N in 2020, where weak SIR variability during the transition period likely reduced the reliability of L-SIR onset detection. Despite these localized exceptions, L-SIR onset was consistently identifiable across most years and latitudes, supporting the stage-based analyses used subsequently.

Figure 4 summarizes the distribution of L-SIR changes within each stage. Each sample represents ΔL-SIR calculated for one grid cell in one year, defined as the mean L-SIR during the last three days of a stage minus the mean L-SIR during the first three days of the same stage. Stage 1 and stage 3 show positive median changes in SIR, with values of approximately 0.22 cm and 0.18 cm, respectively. In contrast, stage 2 is characterized by a pronounced decrease, with a median change of approximately -0.39 cm and a lower whisker extending to -0.79 cm. During stage 1, the positive ΔL-SIR is interpreted not as evidence of physical surface roughening, but as an early L-band response to the pre-ponding transformation of the snow-covered ice surface. Once F_{net} turns positive, the surface progressively warms toward the melting point (Persson, 2012), and the emergence of liquid water within the snowpack begins to alter the dielectric state of the near-surface layer. L-band brightness temperature over snow-covered sea ice is strongly governed by ice temperature and the overlying snow layer (Maaß et al., 2015), making the signal sensitive to these pre-melt thermal and dielectric changes. Because snow wetting is known to affect vertically and horizontally polarized reflectivities unequally, the associated increase in polarization contrast may contribute to a positive ΔL-SIR, reflecting a shift in the near-surface emission state rather than physical roughening of the ice surface (Hong, 2010).

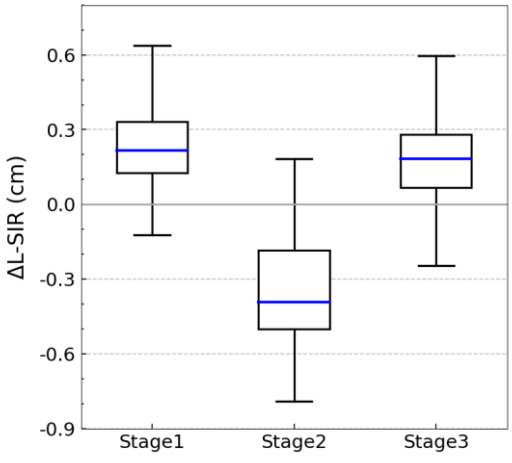

Figure 4: Distribution of stage-wise L-SIR changes (ΔL-SIR). The blue lines indicate the median.

https://doi.org/10.5194/egusphere-2026-2853
Preprint. Discussion started: 5 June 2026

During stage 2, the negative ΔL-SIR is interpreted as an L-band response to the progressive loss of the snowpack and the onset of meltwater redistribution. Throughout this stage, MPF remains below 7.8 %, indicating that the L-SIR decline is not a response to optically detectable ponding, but rather reflects a pre-ponding transition in the surface state. As snow ablation advances, the near-surface dielectric structure that sustained the polarization asymmetry during stage 1 is progressively lost, and the emerging meltwater-influenced surface becomes increasingly specular. This causes vertically and horizontally polarized reflectivities to converge and the retrieved L-SIR to decline (Hong, 2010; Hong and Shin, 2010). Concurrently, meltwater accumulates in topographic depressions and drains laterally toward macroscopic flaws, while vertical percolation through the ice remains limited because refreezing meltwater can block connected pore pathways before a full permeability transition occurs (Polashenski et al., 2012). In this sense, the stage 2 decline marks the transition from a snow-dominated surface signal to one increasingly shaped by meltwater before ponds become optically detectable.

In stage 3, L-SIR initially remains suppressed as melt ponds reach their seasonal maximum, then rises again toward the end of the melt season, yielding a positive ΔL-SIR. This recovery may reflect two contributing processes. As ice permeability increases during the mature melt season, vertical drainage can become the primary meltwater loss pathway, reducing pond coverage and re-exposing bare ice surfaces that are dielectrically more heterogeneous than pond water (Polashenski et al., 2012). Toward the end of the melt season, episodic refreezing can form a thin ice skim over pond surfaces, and early snowfall can cover bare ice. Both would tend to restore near-surface dielectric contrasts and may elevate the retrieved L-SIR (Polashenski et al., 2012; Taylor and Feltham, 2004).

Figure 5 shows the relationship between spatially averaged L-SIR and MPF, where each data point represents the domain-mean values calculated across grid cells assigned to a given stage for a given date. Spatial averaging was applied because the relatively narrow study region exhibited spatially coherent surface conditions. Days on which fewer than 30 % of the grid

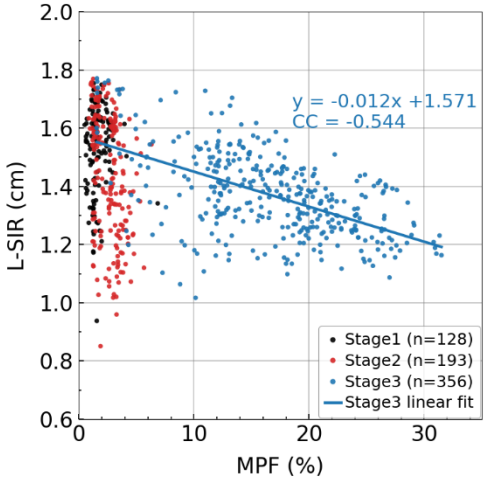

Figure 5: Stage-wise scatterplot of L-SIR and MPF. Each point represents the domain-averaged L-SIR and MPF calculated from grid cells classified into the same stage on a given date. The blue line indicates the linear regression fit for stage 3.

https://doi.org/10.5194/egusphere-2026-2853
Preprint. Discussion started: 5 June 2026

cells were classified as being in the same stage were excluded to ensure spatial representativeness. In stages 1 and 2, no meaningful relationship between L-SIR and MPF is evident. This is consistent with the physical interpretation developed above, in which L-SIR responds primarily to snow-layer conditions and near-surface dielectric changes rather than to pond coverage. Stage 3 shows a markedly different pattern, with a clear negative relationship ($r = -0.544$, slope = -0.012 cm $\%^{-1}$). As MPF increases, L-SIR decreases systematically, indicating that variations in pond coverage become reflected in the L-band signal once ponds occupy a sufficient fraction of the surface. This suggests that surface state changes in midsummer, after the snow cover has been lost, are reflected in the retrieved L-SIR. The contrast between stage 3 and the pre-pond stages indicates that L-SIR is associated with different surface processes across the melt season and should be interpreted accordingly.

Figure 6 shows the Pearson correlation coefficient (r) between L-SIR anomalies and anomalies in seven variables: MPF, F_{net}, LH, SH, LWD, SWD, and Ts. All data were spatially averaged using the same approach as described for Fig. 5. The correlation patterns differ clearly among the three stages, supporting the interpretation that L-SIR responds to different surface processes as the melt season evolves. During Stage 1, L-SIR anomalies show a strong positive correlation with Ts anomalies ($r = 0.60$). This positive relationship suggests that the early increase in L-SIR is closely associated with warming of the snow-covered sea ice surface, although some of this dependence on Ts may arise from the temperature sensitivity of the retrieval itself. The weaker positive correlations with F_{net}, LWD, and SH anomalies suggest that L-SIR tends to increase when warm, moist atmospheric conditions enhance longwave and sensible heat inputs to the surface. These correlations are modest, consistent with stage 1 being a preconditioning period rather than a stage of strong snow ablation. This interpretation is consistent with previous studies showing that Arctic melt onset is closely associated with warm, moist air advection and

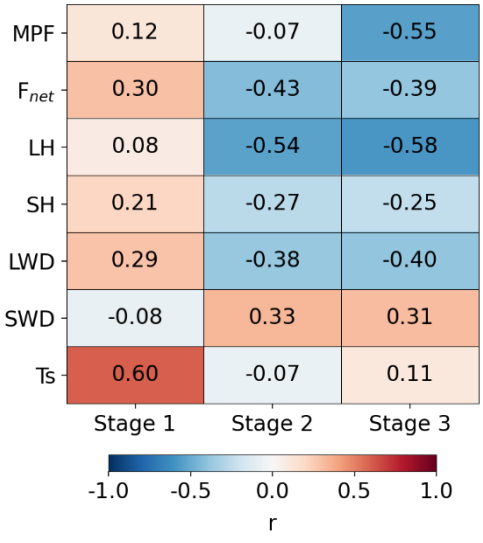

Figure 6: Stage-wise Pearson correlation coefficient (r) between L-SIR anomalies and anomalies in melt-related surface variables, including MPF, F_{net}, LH, SH, LWD, SWD, and Ts.

https://doi.org/10.5194/egusphere-2026-2853
Preprint. Discussion started: 5 June 2026

enhanced LWD, rather than being primarily controlled by shortwave forcing (Persson, 2012; Mortin et al., 2016). The near-zero correlation with SWD is also reasonable, as the remaining thick snow layer in stage 1 has a high albedo and can reflect much of the incoming shortwave radiation.

During stage 2, the relationship between L-SIR anomalies and the energy variables changed markedly from that in stage 1. The correlation with Ts is close to zero, indicating that L-SIR is no longer primarily associated with surface warming once the snow-covered surface has approached the melting point. Instead, L-SIR is negatively correlated with LH, F_{net}, and LWD anomalies, with the strongest negative correlation found for LH (r = -0.54). This pattern suggests that anomalously strong latent heat, net energy, and longwave inputs are associated with lower L-SIR during this stage. Such behavior is consistent with a transition from surface preconditioning to active snow loss. Once the surface is near the melting point, additional energy is more likely to support snow ablation, meltwater production, and meltwater transport than further warming. The positive correlation with SWD should be interpreted cautiously, as it does not necessarily imply that shortwave radiation directly increases SIR. Rather, it may reflect a cloud radiation trade-off, in which clearer conditions increase SWD but reduce LWD and heat input associated with warm, moist air advection. Under these conditions, snowmelt may proceed more slowly than under cloudy, warm, and humid conditions, which could weaken the stage 2 decrease in L-SIR.

During stage 3, the correlation structure shifted from a snowmelt-related signal to a pond-dominated surface signal. L-SIR anomalies show a strong negative correlation with MPF anomalies, indicating that higher pond coverage is associated with lower L-SIR once melt ponds occupy a sufficient fraction of the surface. The negative correlations with most melt-related variables, including anomalies in LH, LWD, and F_{net}, further suggest that lower L-SIR tends to occur under wetter surface conditions with increased energy input. In other words, days with larger LH, LWD, and F_{net} anomalies are likely associated with more active melt pond development or stronger wet-surface conditions, under which L-SIR tends to be lower. As in stage 2, the near-zero correlation with Ts anomalies indicates that Ts is no longer a primary correlate of L-SIR once the surface has remained near the melting point. The positive correlation with SWD anomalies is also interpreted in the same way as in stage 2. It likely reflects cloud–radiation covariability rather than a direct shortwave control on L-SIR, with clearer conditions increasing SWD but providing less favorable warm and moist atmospheric forcing for melt pond development.

5 Discussion

The present study shows that L-SIR is sensitive to an early summer surface transition that precedes the optical emergence of melt ponds. Across seven melt seasons and within the latitudes examined in this study, the mean lag of approximately two weeks between the transition to positive F_{net} and the L-SIR onset, together with the additional lag of roughly four weeks before optically detectable pond formation, indicates that the L-SIR contains information about a pre-pond surface state that is not resolved by optical MPF retrievals alone. The reproducibility of this temporal ordering across years and latitudes makes it unlikely that the signal reflects a single year anomaly and instead suggests that this ordering represents a recurring feature of the central Arctic summer surface.

https://doi.org/10.5194/egusphere-2026-2853
Preprint. Discussion started: 5 June 2026

This temporal sequence is physically consistent with existing process-based descriptions of the Arctic melt season. The cumulative net flux framework of Skyllingstad and Polashenski (2018) emphasizes that F_{net} must first become sufficiently positive to support meltwater accumulation before ponds can form, and Mortin et al. (2016) showed that melt onset is closely tied to the transport of warm, moist air and enhanced LWD rather than to direct shortwave forcing. The present results build on these frameworks by demonstrating that the preconditioning interval can be monitored at daily resolution and with limited sensitivity to cloud cover, which remains the principal limitation of optical retrievals during the central Arctic summer.

The stage-dependent correlations between L-SIR and the surface energy balance variables further support the view that L-SIR reflects physically distinct surface processes across the melt season. The progression from a Ts-dominated regime to a regime associated with latent heat and longwave radiation, and finally to a pond coverage-dominated regime, indicates that L-SIR responds to pre-pond changes such as snow ablation, increasing liquid water content, and lateral meltwater redistribution before ponds become optically detectable. This stage dependence has direct implications for how L-SIR should be interpreted.

Taken together, these results argue for the complementary use of L-SIR and optical MPF. Whereas MPF captures the manifestation of melt ponds once they become optically detectable, L-SIR captures an earlier internal transition of the snow–ice system that precedes and may condition pond formation. Their combined use therefore provides a more complete temporal description of the Arctic summer surface than either product alone and may be particularly useful for evaluating sea ice models that aim to represent the timing of snow ablation, meltwater storage, and pond development.

Several limitations should be acknowledged. The analysis is restricted to a fixed multiyear ice region in the central Arctic, and the extent to which the same sequential structure persists over first-year ice has not been examined here. Pond evolution differs substantially between multiyear and first-year ice in terms of pond size, snow depth, and topographic constraints, and the present results cannot be directly extrapolated to first-year ice without additional analysis. In addition, because the L-SIR retrieval uses Ts as an input variable, part of the stage 1 correlation between L-SIR and Ts may originate in the retrieval formulation. A targeted sensitivity analysis would be needed to separate these contributions. Finally, although the present analysis establishes robust temporal ordering and physically interpretable correlations, it does not by itself demonstrate a causal pathway from the L-SIR transition to pond formation. Whether the L-SIR onset can be used predictively to estimate MPF onset will need to be tested in future work using broader regions, sea ice type.

6 Conclusions

This study demonstrates that L-SIR, retrieved from SMAP brightness temperature polarization differences, captures a reproducible pre-pond surface transition over Arctic multiyear ice. Across 2017–2023, the surface transition followed a consistent sequence: F_{net} became positive first, L-SIR began its sustained decline about two weeks later, and optically detectable melt ponds appeared after an additional four weeks. This timing indicates that L-SIR contains information on the internal evolution of the snow–ice system before melt ponds becomes visible to optical sensors. The results also show that L-

https://doi.org/10.5194/egusphere-2026-2853
Preprint. Discussion started: 5 June 2026

SIR should not be interpreted as a single process variable. Its relationship with surface conditions changes across the melt season, from a temperature-related response in the early stage, to LH and LWD associated response during snow ablation and meltwater redistribution, and finally to a pond coverage-related response after ponds develop. This stage dependence highlights the value of L-SIR as a complementary diagnostic to optical MPF, rather than as a direct proxy for it.

The analysis is limited to a fixed multiyear ice region, and the applicability of this sequence to first-year ice remains unresolved. The temperature dependence of the retrieval and the causal link between L-SIR transition and MPF onset also require further testing. Future work will extend this analysis to broader regions and different ice types to evaluate the robustness and predictive potential of the observed sequence. Despite these limitations, the present study establishes L-SIR as a physically meaningful satellite-derived product for characterizing Arctic summer surface evolution that is not captured by optical MPF alone.

Data availability

The sea ice concentration and sea ice age data used to define the multiyear sea ice study region were obtained from the Arctic Ocean Sea Ice Reanalysis product of the E.U. CMEMS, available at https://doi.org/10.48670/mds-00336.

The melt pond fraction data were taken from the MPD2 dataset provided by the University of Bremen, available at https://data.seaice.uni-bremen.de/MeltPonds-Albedo/MPD2.

The SMAP brightness temperature data used to retrieve L-SIR are available from the NASA NSIDC at https://doi.org/10.5067/M20OXIZHY3RJ.

The surface temperature data used as an additional input for the L-SIR retrieval were obtained from the Arctic Ocean - Sea and Ice Surface Temperature L4 REPROCESSED product of the E.U. CMEMS, available at https://doi.org/10.48670/moi-00123.

ERA5 hourly single-level data are provided by the Copernicus Climate Change Service Climate Data Store and are available at https://doi.org/10.24381/cds.adbb2d47.

Author contributions

SJ completed the experimental setup, produced the figures, and wrote the initial manuscript. SH designed the experimental setup, acquired funding, provided resources, supervised the study, and contributed to reviewing and editing the manuscript.

Competing interests

The authors declare that they have no conflict of interest.

https://doi.org/10.5194/egusphere-2026-2853
Preprint. Discussion started: 5 June 2026

Disclaimer

Copernicus Publications remains neutral with regard to jurisdictional claims made in the text, published maps, institutional affiliations, or any other geographical representation in this paper. While Copernicus Publications makes every effort to include appropriate place names, the final responsibility lies with the authors. Views expressed in the text are those of the authors and do not necessarily reflect the views of the publisher.

Acknowledgements

The authors gratefully acknowledge the anonymous reviewers for their valuable and constructive suggestions.

References

Aparício, S.: Review article: Earth observations of melt ponds on sea ice, The Cryosphere Discuss. [preprint], 2023, 1–65, https://doi.org/10.5194/tc-2023-75, 2023.

Arndt, S., Willmes, S., Dierking, W., and Nicolaus, M.: Timing and regional patterns of snowmelt on Antarctic sea ice from passive microwave satellite observations, J. Geophys. Res. Oceans, 121, 5916–5930, https://doi.org/10.1002/2015JC011504, 2016.

Choudhury, B. J., Schmugge, T. J., Chang, A., and Newton, R. W.: Effect of surface roughness on the microwave emission from soils, J. Geophys. Res., 84, 5699–5706, https://doi.org/10.1029/JC084iC09p05699, 1979.

Comiso, J. C., Cavalieri, D. J., and Markus, T.: Sea ice concentration, ice temperature, and snow depth using AMSR-E data, IEEE Trans. Geosci. Remote Sens., 41, 243–252, https://doi.org/10.1109/TGRS.2002.808317, 2003.

Diamond, R., Schroeder, D., Sime, L. C., Ridley, J., and Feltham, D.: The significance of the melt-pond scheme in a CMIP6 global climate model, J. Clim., 37, 249–268, https://doi.org/10.1175/JCLI-D-22-0902.1, 2024.

Ding, Y., Cheng, X., Liu, J., Hui, F., Wang, Z., and Chen, S.: Retrieval of melt pond fraction over Arctic sea ice during 2000–2019 using an ensemble-based deep neural network, Remote Sens., 12, 2746, https://doi.org/10.3390/rs12172746, 2020.

Eicken, H., Grenfell, T. C., Perovich, D. K., Richter-Menge, J. A., and Frey, K.: Hydraulic controls of summer Arctic pack ice albedo, J. Geophys. Res. Oceans, 109, C08007, https://doi.org/10.1029/2003JC001989, 2004.

Eicken, H., Krouse, H. R., Kadko, D., and Perovich, D. K.: Tracer studies of pathways and rates of meltwater transport through Arctic summer sea ice, J. Geophys. Res. Oceans, 107, 8046, https://doi.org/10.1029/2000JC000583, 2002.

Else, B. G. T., Papakyriakou, T. N., Raddatz, R., Galley, R. J., Mundy, C. J., Barber, D. G., Swystun, K., and Rysgaard, S.: Surface energy budget of landfast sea ice during the transitions from winter to snowmelt and melt pond onset: The importance of net longwave radiation and cyclone forcings, J. Geophys. Res. Oceans, 119, 3679–3693, https://doi.org/10.1002/2013JC009672, 2014.

https://doi.org/10.5194/egusphere-2026-2853
Preprint. Discussion started: 5 June 2026

Entekhabi, D., Njoku, E. G., O'Neill, P. E., Kellogg, K. H., Crow, W. T., Edelstein, W. N., et al.: The Soil Moisture Active Passive (SMAP) mission, Proc. IEEE, 98, 704–716, https://doi.org/10.1109/JPROC.2010.2043918, 2010.

E.U. Copernicus Marine Service Information (CMEMS): Arctic Ocean - Sea and Ice Surface Temperature L4 REPROCESSED [data set], Marine Data Store (MDS), https://doi.org/10.48670/moi-00123, 2026.

Feng, J., Zhang, Y., Cheng, Q., and Tsou, J. Y.: Pan-Arctic melt pond fraction trend, variability, and contribution to sea ice changes, Glob. Planet. Change, 217, 103932, https://doi.org/10.1016/j.gloplacha.2022.103932, 2022.

Fetterer, F. and Untersteiner, N.: Observations of melt ponds on Arctic sea ice, J. Geophys. Res. Oceans, 103, 24821–24835, https://doi.org/10.1029/98JC02034, 1998.

Flocco, D., Schroeder, D., Feltham, D. L., and Hunke, E. C.: Impact of melt ponds on Arctic sea ice simulations from 1990 to 2007, J. Geophys. Res. Oceans, 117, C09032, https://doi.org/10.1029/2012JC008195, 2012.

Hersbach, H., Bell, B., Berrisford, P., Hirahara, S., Horányi, A., Muñoz-Sabater, J., et al.: The ERA5 global reanalysis, Q. J. R. Meteorol. Soc., 146, 1999–2049, https://doi.org/10.1002/qj.3803, 2020.

Hong, S.: Retrieval of refractive index over specular surfaces for remote sensing applications, J. Appl. Remote Sens., 3, 033560, https://doi.org/10.1117/1.3265997, 2009.

Hong, S.: Detection of small-scale roughness and refractive index of sea ice in passive satellite microwave remote sensing, Remote Sens. Environ., 114, 1136–1140, https://doi.org/10.1016/j.rse.2009.12.015, 2010.

Hong, S. and Shin, I.: Global trends of sea ice: Small-scale roughness and refractive index, J. Clim., 23, 4669–4676, https://doi.org/10.1175/2010JCLI3697.1, 2010.

Istomina, L., Niehaus, H., and Spreen, G.: Updated Arctic melt pond fraction dataset and trends 2002–2023 using ENVISAT and Sentinel-3 remote sensing data, Cryosphere, 19, 83–105, https://doi.org/10.5194/tc-19-83-2025, 2025.

Jo, S., Kim, H. C., Kwon, Y. J., and Hong, S.: Circumpolar thin Arctic sea ice thickness and small-scale roughness retrieval using Soil Moisture and Ocean Salinity and Soil Moisture Active Passive observations, Remote Sens., 11, 2835, https://doi.org/10.3390/rs11232835, 2019.

Kaleschke, L., Tian-Kunze, X., Maaß, N., Mäkynen, M., and Drusch, M.: Sea ice thickness retrieval from SMOS brightness temperatures during the Arctic freeze-up period, Geophys. Res. Lett., 39, L05501, https://doi.org/10.1029/2012GL050916, 2012.

Karagali, I., Englyst, P., Kolbe, W., and Høyer, J.: Copernicus marine product user manual for Arctic Ocean Sea and Sea-Ice Surface Temperature Products-011016021, Issue 4.0, E.U. Copernicus Marine Service, 2025.

Landy, J., Ehn, J., Shields, M., and Barber, D.: Surface and melt pond evolution on landfast first-year sea ice in the Canadian Arctic Archipelago, J. Geophys. Res. Oceans, 119, 3054–3075, https://doi.org/10.1002/2013JC009617, 2014.

Lange, B. A., Beckers, J. F., Casey, J. A., and Haas, C.: Airborne observations of summer thinning of multiyear sea ice originating from the Lincoln Sea, J. Geophys. Res. Oceans, 124, 243–266, https://doi.org/10.1029/2018JC014383, 2019.

Liu, J., Song, M., Horton, R. M., and Hu, Y.: Revisiting the potential of melt pond fraction as a predictor for the seasonal Arctic sea ice extent minimum, Environ. Res. Lett., 10, 054017, https://doi.org/10.1088/1748-9326/10/5/054017, 2015.

https://doi.org/10.5194/egusphere-2026-2853
Preprint. Discussion started: 5 June 2026

Lüthje, M., Feltham, D. L., Taylor, P. D., and Worster, M. G.: Modeling the summertime evolution of sea-ice melt ponds, J. Geophys. Res. Oceans, 111, C02001, https://doi.org/10.1029/2004JC002818, 2006.

Maaß, N., Kaleschke, L., Tian-Kunze, X., and Drusch, M.: Snow thickness retrieval over thick Arctic sea ice using SMOS satellite data, Cryosphere, 7, 1971–1989, https://doi.org/10.5194/tc-7-1971-2013, 2013.

Maaß, N., Kaleschke, L., Tian-Kunze, X., and Tonboe, R. T.: Snow thickness retrieval from L-band brightness temperatures: A model comparison, Ann. Glaciol., 56, 9–17, https://doi.org/10.3189/2015AoG69A886, 2015.

Mohammed, P. N., Aksoy, M., Piepmeier, J. R., Johnson, J. T., and Bringer, A.: SMAP L-band microwave radiometer: RFI mitigation prelaunch analysis and first year on-orbit observations, IEEE Trans. Geosci. Remote Sens., 54, 6035–6047, https://doi.org/10.1109/TGRS.2016.2580459, 2016.

Mortin, J., Svensson, G., Graversen, R. G., Kapsch, M.-L., Stroeve, J. C., and Boisvert, L. N.: Melt onset over Arctic sea ice controlled by atmospheric moisture transport, Geophys. Res. Lett., 43, 6636–6642, https://doi.org/10.1002/2016GL069330, 2016.

Niehaus, H., Istomina, L., Nicolaus, M., Tao, R., Malinka, A., Zege, E., and Spreen, G.: Melt pond fractions on Arctic summer sea ice retrieved from Sentinel-3 satellite data with a constrained physical forward model, Cryosphere, 18, 933–956, https://doi.org/10.5194/tc-18-933-2024, 2024.

Niehaus, H., Spreen, G., Birnbaum, G., Istomina, L., Jäkel, E., Linhardt, F., Neckel, N., Fuchs, N., Nicolaus, M., Sperzel, T., Tao, R., Webster, M., and Wright, N.: Sea ice melt pond fraction derived from Sentinel-2 data: along the MOSAiC drift and Arctic-wide, Geophys. Res. Lett., 50, e2022GL102102, https://doi.org/10.1029/2022GL102102, 2023.

Niehaus, H., Spreen, G., Istomina, L., and Nicolaus, M.: Regional and seasonal evolution of melt ponds on Arctic sea ice, Cryosphere, 19, 3915–3938, https://doi.org/10.5194/tc-19-3915-2025, 2025.

O'Neill, P. E., Chan, S., Njoku, E. G., Jackson, T., Bindlish, R., Chaubell, J., and Colliander, A.: SMAP Enhanced L3 Radiometer Global and Polar Grid Daily 9 km EASE-Grid Soil Moisture [data set], NASA NSIDC, v6, https://doi.org/10.5067/M20OXIZHY3RJ, 2023.

O'Neill, P., Chan, S., Njoku, E., Jackson, T., and Bindlish, R.: Algorithm theoretical basis document level 2 & 3 soil moisture (passive) data products, Tech. Rep. JPL D-66480, JPL, Caltech, Pasadena, CA, USA, 2021.

Perovich, D. K. and Polashenski, C.: Albedo evolution of seasonal Arctic sea ice, Geophys. Res. Lett., 39, L08501, https://doi.org/10.1029/2012GL051432, 2012.

Persson, P. O. G.: Onset and end of the summer melt season over sea ice: Thermal structure and surface energy perspective from SHEBA, Clim. Dyn., 39, 1349–1371, https://doi.org/10.1007/s00382-011-1196-9, 2012.

Piepmeier, J. R., Johnson, J. T., Mohammed, P. N., Bradley, D., Ruf, C., Aksoy, M., et al.: Radio-frequency interference mitigation for the Soil Moisture Active Passive microwave radiometer, IEEE Trans. Geosci. Remote Sens., 52, 761–775, https://doi.org/10.1109/TGRS.2013.2281266, 2014.

Polashenski, C., Perovich, D., and Courville, Z.: The mechanisms of sea ice melt pond formation and evolution, J. Geophys. Res. Oceans, 117, C01001, https://doi.org/10.1029/2011JC007231, 2012.

https://doi.org/10.5194/egusphere-2026-2853
Preprint. Discussion started: 5 June 2026

Rantanen, M., Karpechko, A. Y., Lipponen, A., Nordling, K., Hyvärinen, O., Ruosteenoja, K., Vihma, T., and Laaksonen, A.: The Arctic has warmed nearly four times faster than the globe since 1979, Commun. Earth Environ., 3, 168, https://doi.org/10.1038/s43247-022-00498-3, 2022.

Rösel, A., Kaleschke, L., and Birnbaum, G.: Melt ponds on Arctic sea ice determined from MODIS satellite data using an artificial neural network, Cryosphere, 6, 431–446, https://doi.org/10.5194/tc-6-431-2012, 2012.

Schröder, D., Feltham, D. L., Flocco, D., and Tsamados, M.: September Arctic sea-ice minimum predicted by spring melt-pond fraction, Nat. Clim. Chang., 4, 353–357, https://doi.org/10.1038/nclimate2203, 2014.

Serreze, M. C. and Meier, W. N.: The Arctic's sea ice cover: trends, variability, predictability, and comparisons to the Antarctic, Ann. N. Y. Acad. Sci., 1436, 36–53, https://doi.org/10.1111/nyas.13856, 2019.

Skyllingstad, E. D., Paulson, C. A., and Perovich, D. K.: Simulation of melt pond evolution on level ice, J. Geophys. Res. Oceans, 114, C12019, https://doi.org/10.1029/2009JC005363, 2009.

Skyllingstad, E. D. and Polashenski, C.: Estimated heat budget during summer melt of Arctic first-year sea ice, Geophys. Res. Lett., 45, 11,789–11,797, https://doi.org/10.1029/2018GL080349, 2018.

Skyllingstad, E. D., Shell, K. M., Collins, L., and Polashenski, C.: Simulation of the melt season using a resolved sea ice model with snow cover and melt ponds, J. Geophys. Res. Oceans, 120, 5194–5215, https://doi.org/10.1002/2014JC010569, 2015.

Stroeve, J. C., Markus, T., Boisvert, L., Miller, J., and Barrett, A.: Changes in Arctic melt season and implications for sea ice loss, Geophys. Res. Lett., 41, 1216–1225, https://doi.org/10.1002/2013GL058951, 2014.

Taylor, P. D. and Feltham, D. L.: A model of melt pond evolution on sea ice, J. Geophys. Res. Oceans, 109, C12007, https://doi.org/10.1029/2004JC002361, 2004.

Walsh, J. E., Chapman, W. L., and Portis, D. H.: Arctic cloud fraction and radiative fluxes in atmospheric reanalyses, J. Clim., 22, 2316–2334, https://doi.org/10.1175/2008JCLI2213.1, 2009.

Williams, T., Korosov, A., Rampal, P., and Ólason, E.: Presentation and evaluation of the Arctic sea ice forecasting system neXtSIM-F, Cryosphere, 15, 3207–3227, https://doi.org/10.5194/tc-15-3207-2021, 2021.